Volume 27
Number 26
14 July 2025
Pages 13757–14156

PCCP

Physical Chemistry Chemical Physics

rsc.li/pccp

25 YEARS ANNIVERSARY

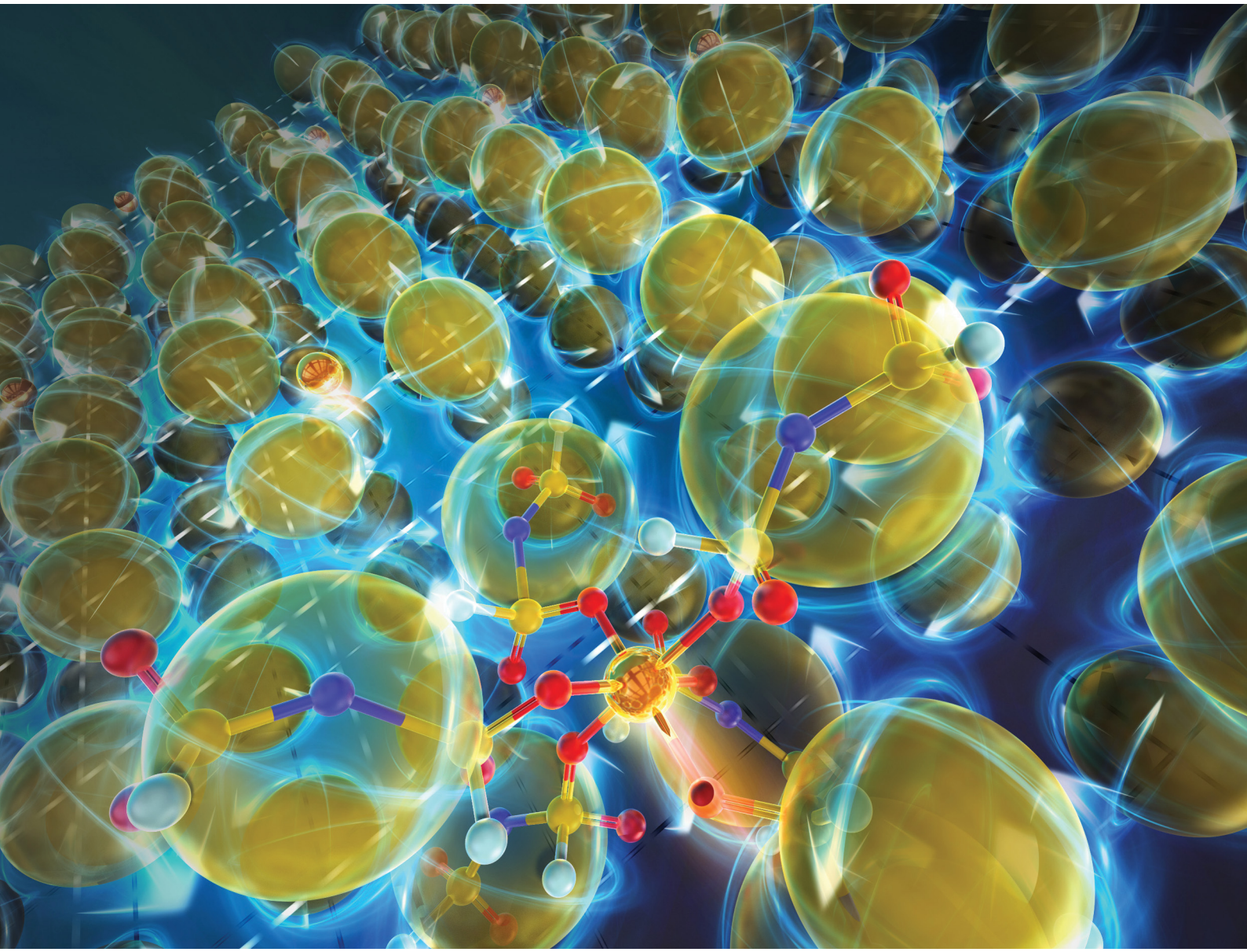

ISSN 1463-9076

ROYAL SOCIETY OF CHEMISTRY

PAPER

Masahiro Yoshizawa-Fujita *et al.*

Enhanced ion-transport characteristics of pyrrolidinium-based electrolytes with $Mg(FSA)_2$

PCCP Owner Societies

PCCP

ROYAL SOCIETY OF CHEMISTRY

PAPER

View Article Online
View Journal | View Issue

Cite this: *Phys. Chem. Chem. Phys.*, 2025, **27**, 13826

Enhanced ion-transport characteristics of pyrrolidinium-based electrolytes with $Mg(FSA)_2$†

Yoshifumi Hirotsu, Mizuki Kimura, Shinkoh Nanbu, Yuko Takeoka, Masahiro Rikukawa and Masahiro Yoshizawa-Fujita *

Organic ionic plastic crystals (OIPCs) are gaining attention as next-generation solid electrolytes owing to their excellent thermal and electrochemical stability and high ionic conductivity. However, reports on the application of OIPCs to Mg electrolytes are limited. In this study, Mg-ion conductors based on the bis(fluorosulfonyl)amide (FSA) anion were prepared by adding $Mg(FSA)_2$ to the pyrrolidinium-based OIPC *N,N*-diethylpyrrolidinium bis(fluorosulfonyl)amide ($[C_2epyr][FSA]$). We then evaluated the Mg transference number ($t_{Mg^{2+}}$), ionic conductivity, phase transition behaviour, and Mg-ion solvation number (with FSA anions) of the resultant materials to investigate how the Mg-salt concentration influences their ionic conduction characteristics and thermal stability. The $[C_2epyr][FSA]/Mg(FSA)_2$ composites were solid at room temperature when the Mg-salt concentration was below 10 mol% but became liquid at concentrations above 10 mol%. Among the composites investigated in this study, $[C_2epyr][FSA]/Mg(FSA)_2$ (10 mol%) showed the highest ionic conductivity, which reached 1.78×10^{-3} S cm^{-1} at 25 °C. When the Mg-ion concentration was above 10 mol%, the $t_{Mg^{2+}}$ of $[C_2epyr][FSA]/Mg(FSA)_2$ was below 0.16. By contrast, when the Mg-salt concentration was below 10 mol%, the $t_{Mg^{2+}}$ of $[C_2epyr][FSA]/Mg(FSA)_2$ was 0.26 or higher, surpassing those of the liquid-state composites. Cyclic voltammetry measurements revealed that $[C_2epyr][FSA]/Mg(FSA)_2$ (5 mol%) exhibited the redox behaviour of Mg at 60 °C. These results indicate that FSA-anion-based composites function more effectively as Mg-ion conductors in the solid state than in the liquid state.

Received 11th April 2025,
Accepted 3rd May 2025

DOI: 10.1039/d5cp01386k

rsc.li/pccp

Introduction

Lithium-ion secondary batteries are highly promising energy storage devices owing to their high energy density, excellent cycling characteristics, and enhanced reliability. However, challenges such as safety concerns, high costs, and resource scarcity remain unresolved.[1,2] These issues can be overcome by the development of alternative devices with abundant resources and economic feasibility, particularly Mg-ion secondary batteries (MIBs).[3] Mg, a divalent metal, can offer a higher volumetric capacity (3833 mA h cm^{-3}) than Li (2046 mA h cm^{-3}). As the fifth most abundant element in the Earth's crust, Mg holds significant potential as a next-generation energy storage material.[4,5] Additionally, Mg anodes are known to be less susceptible to dendrite formation than Li anodes.[6] Matsui reported that Mg-metal deposition exhibits high coulombic efficiency and uniformity, which suppresses dendrite growth, because it does not form a solid electrolyte interphase (SEI) layer.[7] Research on MIBs has recently accelerated, and numerous reports on the technology have been published. For example, Lethesh *et al.* developed a Mg electrolyte by combining Mg bis(diisopropyl)amide and 1-ethyl-3-methylimidazolium tetrachloroaluminate in a 1 : 2 molar ratio. Using a Mo_6S_8 cathode in a full-cell test, the authors achieved a cycling life of over 300 cycles while maintaining a capacity retention rate of over 80%.[8] Nevertheless, the development of suitable electrolytes and a deeper understanding of the fundamental mechanisms of MIBs remain key challenges in the field.[9]

Solid electrolytes have received increased attention in recent years for their potential to improve the safety of energy storage devices because they eliminate the risk of liquid leakage.[10–12] Polymer-based electrolytes, particularly those based on poly(ethylene oxide) (PEO), have been extensively studied for decades. Various Mg salts have been incorporated into PEO matrices to optimize ionic conductivity. Among these, the $PEO/Mg(NO_3)_2$ system exhibits a higher ionic conductivity reported to date at room temperature, reaching 1.34×10^{-5} S cm^{-1}.[13] Polymer blending is an effective strategy for tuning chain mobility. By combining different polymers, it is possible to achieve a wide range of physical and chemical properties. In a system where

Department of Materials & Life Sciences, Sophia University, 7-1 Kioi-cho Chiyoda-ku, Tokyo 102-8554, Japan. E-mail: masahi-f@sophia.ac.jp

† Electronic supplementary information (ESI) available: Raman spectra, activation energy of ionic conductivity, DC polarization curves, Mg transference number, isothermal TG profiles, and XPS spectra. See DOI: https://doi.org/10.1039/d5cp01386k

poly(vinylpyrrolidone) (PVP) is added to PEO/$Mg(NO_3)_2$, an ionic conductivity of 5.8×10^{-4} S cm^{-1} at room temperature and a Mg transference number of 0.33 have been reported. Furthermore, this electrolyte exhibits stable operation even at 4 V.[14] However, the realization of stable operation at room temperature remains a challenge.[15] Poly(ethylene carbonate) (PEC)-based electrolytes have also been investigated, achieving an ionic conductivity of 5.2×10^{-5} S cm^{-1} at 90 °C in a system doped with $Mg(ClO_4)_2$.[16] Our group has been investigating organic ionic plastic crystals (OIPCs) as solid electrolytes for rechargeable batteries. OIPCs are a novel class of solid electrolytes that exhibit a plastic crystal (PC) phase, which is an intermediate state between solid and liquid. In the PC phase, the constituent ions maintain a three-dimensional positional order while freely rotating, leading to orientational disorder. Owing to their ionic nature, OIPCs are characterised by non-flammability, low volatility, high conductivity, and excellent electrochemical stability.[17,18] Yamada *et al.* synthesised pyrrolidinium-based OIPCs with different side-chain structures and investigated the impact of the cationic side chain on the ionic conductivity of the resulting materials. The authors found that the ionic conductivities of *N,N*-dimethylpyrrolidinium bis(fluorosulfonyl)amide, *N*-ethyl-*N*-methylpyrrolidinium bis(fluorosulfonyl)amide ([C_2mpyr][FSA]), and *N,N*-diethylpyrrolidinium bis(fluorosulfonyl)amide ([C_2epyr][FSA]) (Fig. 1) at 25 °C were 1.3×10^{-8}, 1.2×10^{-6}, and 9.6×10^{-6} S cm^{-1}, respectively; among the OIPCs investigated, [C_2epyr][FSA] exhibited the highest conductivity.[19] The authors further reported that modifying the cationic side chains may present a design strategy for electrolytes.

Yoshizawa-Fujita *et al.* studied pyrrolidinium-based OIPCs with five different sulfonylamide anions and reported that variations in anion species significantly influenced the physical state and ionic conductivity of the resultant composites. The authors found a correlation between ionic conductivity and cation–anion interaction as well as ionic radius ratio.[20] However, research on molecular design strategies to enable the use of OIPCs as electrolytes remains limited, and further studies are needed to expand their practical applications. Materials informatics has facilitated the molecular design of highly conductive OIPCs,[21] deepening the understanding of the correlation between molecular structure and physicochemical properties. The development of OIPC-based devices has also progressed. Sunarso *et al.* conducted charge–discharge measurements on composites of *N*-ethyl-*N*-methylpyrrolidinium bis(trifluoromethylsulfonyl)amide ([C_2mpyr][TFSA]) and 10 mol% LiTFSA. In a Li|OIPC/Li-salt composite|$LiFePO_4$ cell, discharge capacities reaching 126 mA h g^{-1} at 50 °C and 153 mA h g^{-1} at 80 °C, as well as excellent cycling retention and high-rate performance, were obtained.[22] OIPCs have diverse applications, and supercapacitors assembled using mesoporous carbon electrodes and [C_2mpyr][FSA]/LiFSA electrolytes have been reported.[23] These supercapacitors maintained a capacitance retention rate of approximately 100% up to 20C, which is comparable with that of cells containing organic electrolyte solutions. OIPC electrolytes are also considered promising materials for the development of all-solid-state high-voltage supercapacitors. In recent years, the addition of polyvinylidene fluoride (PVDF) to OIPC-based electrolytes has been reported to enhance their ionic conductivity.[24] Yanyu *et al.* developed an OIPC-based composite electrolyte composed of *N*-ethyl-*N*-methylpyrrolidinium bis(trifluoromethylsulfonyl)amide ([C_2mpyr][TFSA]), LiTFSA, and PVDF using a simple solution-casting strategy, and evaluated a composite membrane containing 30 wt% PVDF in $Li_{0.33}[C_2mpyr]_{0.67}$[TFSA] as a solid electrolyte in a $LiFePO_4$/Li cell. The cell exhibited a high specific discharge capacity of 149 mA h g^{-1} at 0.1C and demonstrated excellent cycling stability over 440 cycles, with a capacity retention of 89% at 0.5C and 50 °C.[25]

At present, reports on the application of OIPCs to Mg electrolytes are limited. In a previous study, we reported the preparation of $Mg(TFSA)_2$-doped pyrrolidinium-based OIPCs ([C_2epyr][FSA] and *N,N*-diethylpyrrolidinium bis(trifluoromethylsulfonyl)amide ([C_2epyr][TFSA])).[26] The redox reaction of Mg was observed in these FSA-anion-based OIPC/Mg salt composites, suggesting that FSA anions play a crucial role in Mg electrochemistry. However, prior studies involved only mixed TFSA and FSA anions, and no evaluation of FSA anions alone has been conducted. In this study, we added $Mg(FSA)_2$ to [C_2epyr][FSA], which has relatively high ionic conductivity, and evaluated the characteristics of the resulting Mg-ion conductor. This report is the first to focus solely on Mg-ion conductors composed exclusively of FSA anions, allowing a detailed examination of the effect of FSA anions on Mg-ion conduction.

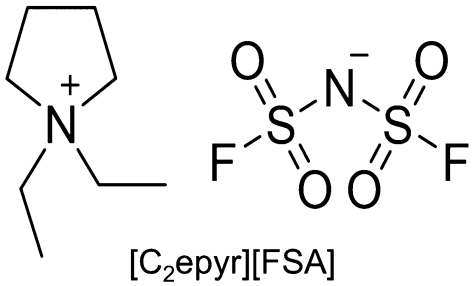

Fig. 1 Chemical structure of the pyrrolidinium-based OIPC used in this study.

Experimental

Materials

1-Ethylpyrrolidine (98%) and 2-iodopropane (>99.0%) were purchased from Tokyo Chemical Industry Co., Ltd. Iodoethane (>98.0%) and acetonitrile (AN, 99.8%) were purchased from FUJIFILM Wako Pure Chemical Corp. All reagents were purified prior to use. Lithium bis(fluorosulfonyl)amide (LiFSA, 99%) was purchased from Kishida Chemical Co., Ltd. Mg bis(fluorosulfonyl)amide acetonitrile solvate ($Mg(FSA)_2 \cdot 6AN$, 98%) was purchased from PROVISCO CS Ltd. All solvents were purchased from Kanto Chemical Co., Inc. or FUJIFILM Wako Pure Chemical Corp. and purified as necessary.

Synthesis of the OIPC

[C_2epyr][FSA] was synthesised according to previously reported methods.[19,20] Briefly, an aqueous solution of LiFSA was added

dropwise to an aqueous solution of $[C_2epyr]I$. The chemical structure of the resulting OIPC was confirmed by ^1H nuclear magnetic resonance (NMR) spectroscopy (Bruker AVANCE III HD NanoBay 400 MHz), fast atom bombardment mass spectrometry (JMS-T100LC), and elemental analysis (JM11, J-SCIENCE LAB Co. Ltd). The water content of the obtained $[C_2epyr][FSA]$ was determined using Karl Fischer coulometric titration with oven (MKH-710, Kyoto Electronics Manufacturing Co., Ltd) to be below 10 ppm before use.

Preparation of OIPC/$Mg(FSA)_2$ composites

The OIPC and $Mg(FSA)_2$·6AN were weighed and stirred at 25 °C for 72 h to prepare the OIPC/$Mg(FSA)_2$ composites in an Ar-filled glove box. AN was removed by drying under reduced pressure at 25 °C for 72 h. In this study, the $[C_2epyr][FSA]$/$Mg(FSA)_2$ composites are referred to as $[C_2epyr]Mg$-x, where x represents the concentration (mol%) of $Mg(FSA)_2$.

Thermal stability

Isothermal thermogravimetry (TG) measurements were performed on a TG-DTA7200 instrument (Hitachi High-Tech) at 60, 80, or 100 °C under a N_2 atmosphere for 2 h. Samples were weighed into Al pans under Ar gas in a glove box.

Phase transition behaviour

The phase transition behaviours of the composites were investigated by differential scanning calorimetry (DSC) using a DSC7020 instrument (Hitachi High-Tech) at a scan rate of 10 °C min^{-1}. Samples were sealed in Al pans under an Ar atmosphere in a glove box. The reported data were obtained from the second heating scan. Measurements were obtained between −150 and 150 °C.

Raman spectroscopy

The Raman spectra of $[C_2epyr]Mg$-x were measured to investigate the dissolution state of Mg ions in these materials. Sealed sample tubes were prepared under an Ar atmosphere in a glove box. The measurements were performed with a Jasco PR-1w Palmtop Raman spectrometer (JASCO Corp.) using an exposure time of 2 s and 32 accumulations. The laser excitation wavelength was set to 785 nm, and the laser power was adjusted to 50 mW. Spectral data were collected over the range of 3000–200 cm^{-1}. The raw Raman spectra were normalised based on appropriate Raman bands arising from the cation ($[C_2epyr]^+$). Data fitting was performed using OriginPro 2023b. Peak separation and fitting were performed using Gaussian functions.

Optimisation of molecular structures using the *ab initio* self-consistent field (SCF) and Møller–Plesset second-order perturbation (MP2) theory methods

Quantum chemical calculations were performed to visualise the structure of the Mg^{2+}–FSA^- complex. The basis set used was aug-cc-pVDZ, which is a correlation-consistent valence double-zeta-type Gaussian basis set that includes polarisation functions on each atom and additional diffuse functions to account for dispersion. The molecular geometry optimisations were performed using the self-consistent field (SCF) method based on the Hartree–Fock approach, and then the electron correlation energy was corrected by the second-order Møller–Plesset perturbation expansion (MP2) method. Gaussian 16 program package was employed for the all *ab initio* computations.[27]

Ionic conductivity

The ionic conductivities of $[C_2epyr]Mg$-x were measured using a VSP-300 impedance analyser (BioLogic) and SU-261 temperature-controlled chamber (ESPEC Corp.). A doughnut-shaped spacer made from Kapton tape (No. 650S-P, Kenis Co., Ltd) with an outer diameter of 24 mm, an inner diameter of 5 mm, and a thickness of 250 μm was attached to a stainless steel electrode. The sample was assembled in a 2032-type coin cell (Hohsen Corp.) in a glove box under an Ar atmosphere. The cell was placed in the thermostatic chamber and measured after stabilisation for 30 min over the frequency range of 100 mHz–1 MHz and an applied voltage of 10 mV over temperatures ranging from −30 to 100 °C. This procedure was repeated for each sample. The activation energy of ionic conductivity was calculated using eqn (1):

$$\sigma = A\exp(-E_a/RT) \quad (1)$$

where A is a pre-exponential factor and E_a, R, and T are the activation energy, universal gas constant, and temperature, respectively.

Mg transference number

$t_{Mg^{2+}}$ was measured electrochemically according to the Vincent–Bruce method.[28] The surface of Mg plates (MG-273408, 0.25 × 50 × 50 mm^3, 99.9%, Nilaco Corp.) was polished with a razor in a glove box under an Ar atmosphere to prepare the plates for use. After stabilising the measurement cell at 25 °C for 24 h, measurements were conducted at 25 °C using a VSP-300 instrument (BioLogic). DC polarisation was performed to examine $t_{Mg^{2+}}$ in $[C_2epyr]Mg$-x *via* the symmetric polarisation procedure devised by Karol.[29] The temperature was controlled using a TB-1 thermostatic chamber (BAS Inc.). $t_{Mg^{2+}}$ was calculated using eqn (2):

$$t_{Mg^{2+}} = I_s/I_0, \quad (2)$$

where I_s and I_0 represent the stationary and initial currents, respectively.

Cyclic voltammetry

Cyclic voltammetry (CV) was performed to investigate the redox reactions of Mg in the electrolyte. A doughnut-shaped spacer made from Kapton tape (No. 650S-P, Kenis Co., Ltd) with an outer diameter of 24 mm, an inner diameter of 5 mm, and a thickness of 50 μm was attached to a Pt electrode. The sample was assembled in a 2032-type coin cell (Hohsen Corp.) in a glove box under an Ar atmosphere. CV was performed at 60 °C using a VSP-300 instrument (BioLogic) in a TB-1 thermostatic chamber (BAS Inc.). The measurements were conducted over the voltage range of −0.50 to 2.0 V, and the scan rate was 10 mV s^{-1}. A Pt electrode was used as the working electrode, and Mg electrodes were used as the reference and counter electrodes.

X-ray photoelectron spectroscopy

X-ray photoelectron spectroscopy (XPS) was conducted using an ULVAC-PHI instrument (PHI 5000 VersaProbe II) with a monochromatic Al Kα X-ray source. The binding energies of the XPS spectra were calibrated by setting the C 1s peak to 284.6 eV. The Pt electrodes obtained after CV were washed with dichloromethane, and their surfaces were scanned.

Results and discussion

Thermal behaviour

Fig. 2 shows the DSC profiles of the OIPC/Mg-salt composites. [C_2epyr][FSA] exhibited a solid–solid phase transition temperature (T_{s-s}) of −34.4 °C and a melting point (T_m) of 130 °C, which are consistent with previously reported data.[26] Generally, the temperature range from T_m to the first T_{s-s} is defined as phase I. For [C_2epyr][FSA], phase I ranged from −34.4 to 130 °C, covering a wide range of temperatures, including room temperature. OIPCs, despite being solid, exhibit high entropy owing to the disorder of their constituent ions; hence, they tend to have low entropy of fusion (ΔS_f). Timmermans reported that the ΔS_f of PCs is typically below 20 J K^{-1} mol^{-1},[30] and the ΔS_f of [C_2epyr][FSA] (8.2 J K^{-1} mol^{-1}) was consistent with this criterion. OIPCs containing FSA^- demonstrate relatively low ΔS_f values, indicating a high degree of disorder in phase I.[31]

The addition of alkali metal salts to OIPCs generally induces complex phase behaviours, leading to solid, biphasic, or liquid composites.[32] In this study, the addition of $Mg(FSA)_2$ significantly altered the phase behaviour of [C_2epyr]Mg-x; specifically, the composite remained solid when x = 2.5–7.5 and became liquid when $x \geq 10$. The solid-state composites (x = 2.5, 5, 7.5) exhibited broad T_m values of approximately 120, 110, and 100 °C, respectively. The addition of $Mg(FSA)_2$ lowered the T_m of [C_2epyr][FSA]. These T_m values could not be detected as clear peaks even at different heating rates.

Similar phenomena have been observed by Kufel *et al.* when NaFSA was added to *N*-isopropyl-*N*-methylpyrrolidinium bis(fluorosulfonyl)amide,[32] indicating that alkali metal-salt addition promotes T_m reduction and liquid complex formation. The behaviour of the OIPC/Mg salt composites in this study may also be attributed to the system heterogeneity caused by Mg-ion addition. Additionally, in [C_2epyr]Mg-x with $x \leq 10$, a peak corresponding to T_{s-s} was observed at approximately −35 °C when x = 10. This result is consistent with the findings of Ueda *et al.*, who studied composites of *N*-ethyl-*N*-methylpyrrolidinium tetrafluoroborate ([C_2mpyr][BF_4]) with Li tetrafluoroborate ($LiBF_4$).[33] They confirmed the co-existence of the OIPC and [C_2mpyr][BF_4]/$LiBF_4$ composite phases at low concentrations (below 50 mol%), suggesting that some OIPC components remained

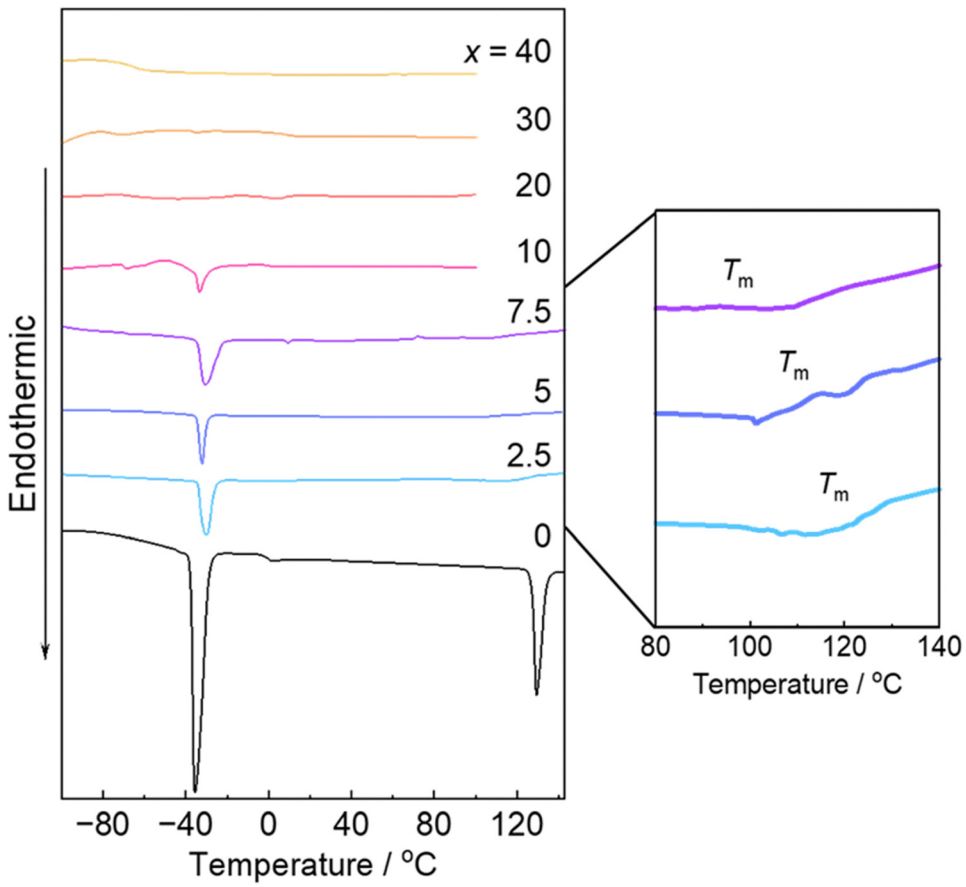

Fig. 2 DSC profiles of [C_2epyr]Mg-x. The figure on the right shows the DSC profiles near the melting point of [C_2epyr]Mg-x (x = 2.5, 5, 7.5).

even in the liquid state. Furthermore, at Mg-salt concentrations exceeding 30 mol%, a glass transition temperature (T_g) was observed, with T_g values of −80 and −73 °C noted when x = 30 and 40, respectively. Similar trends have been reported in [C_2mim][FSA] (1-ethyl-3-methylimidazolium) and NaFSA composites,[34,35] which were attributed to enhanced dynamic cross-linking, ion pairing, and reduced overall molecular dynamics.

Dissociation state of the Mg salt

Fig. S1 (ESI†) presents the Raman spectra of the OIPC and OIPC/Mg-salt composites. $TFSA^-$ coordinates with Mg^{2+} in electrolytes are known to form complex ions.[36] In the Li system, FSA^- can be assigned to peaks similar to those of $TFSA^-$,[37] with FSA^- exhibiting characteristic peaks attributed to the symmetric stretching vibration of the N–S bond (ν_s(N–S)) at around 730 cm^{-1} and the symmetric stretching vibration of the S═O bond (ν_s(S═O)) at around 1220 cm^{-1}.[26,38] In this study, the ν_s(S═O) band at 1230 cm^{-1} was used as a reference because the 730 cm^{-1} band overlaps with those of the pyrrolidinium cation. Coordination with Mg^{2+} has been reported to shift ν_s(S═O) to a higher wavenumber.[26] Ideally, Raman spectral peaks follow a Lorentzian function, but amorphous materials may exhibit Gaussian behaviour. Hence, Gaussian peak fitting was performed to accurately separate the peak components. The analysis revealed that the Raman spectra could be deconvoluted into two components: free FSA^- (uncoordinated) and bound FSA^- (coordinated with Mg^{2+}). As the Mg-salt concentration increased, the proportion of bound FSA increased whereas that of free FSA decreased (Table S1, ESI†), suggesting a reduction in FSA^- dissociation owing to interactions with Mg^{2+}. The shift in the Raman spectrum is associated with the formation of Mg^{2+}–FSA^- aggregates. To determine the solvation number of Mg^{2+}, we applied the method reported by Fujii *et al.*[38,39] to the Raman spectra at 1230 cm^{-1}. The plot of I_f/m_{Mg} *versus* m_T/m_{Mg} (Fig. 3) exhibits a linear relationship; here, I_f represents the integrated intensity of free FSA, m_{Mg} denotes the concentration of Mg ions, and m_T corresponds to the total

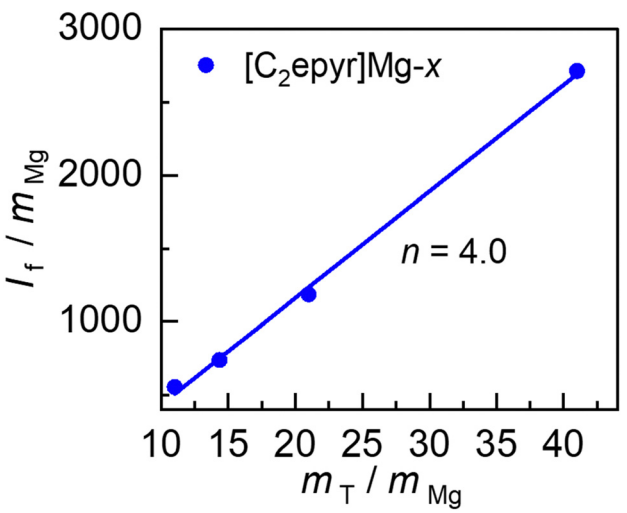

Fig. 3 Plots of I_f/m_{Mg} *versus* m_T/m_{Mg} for the 1220 cm^{-1} band of [C_2epyr]Mg-x. n: solvation number.

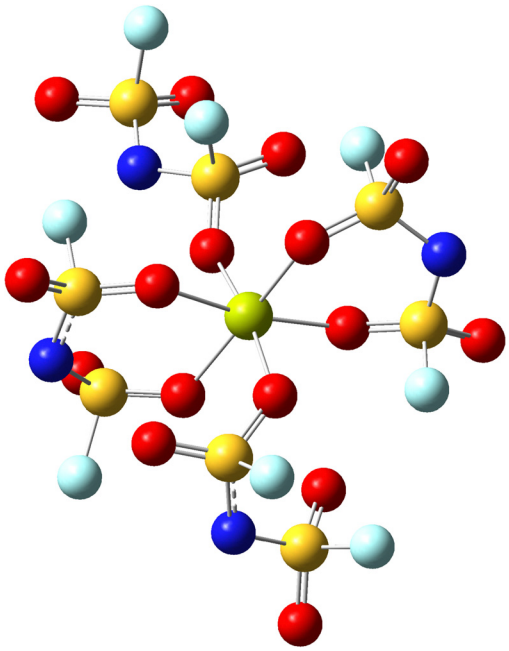

Fig. 4 Typical Mg^{2+} solvation structure extracted from the snapshot. Light green: Mg, red: O, blue: N, yellow: S, light blue: F.

concentration of FSA^-. The solvation number of Mg^{2+} in [C_2epyr]Mg-x was determined to be 4.0. This value is higher than that of Li^+ in [C_2mim][FSA]/LiFSA composites, as reported by Fujii *et al.*[38]

Timo *et al.* previously reported a solvation number of 2.7 for Na^+ in composites of *N*-butyl-*N*-methylpyrrolidinium bis(fluorosulfonyl)amide and NaFSA;[40] this value has also been observed in [C_2epyr][FSA]/NaFSA composites.[41] Compared with these results, the relatively high solvation number of Mg^{2+} obtained in this study suggests strong interactions between Mg^{2+} and FSA^-, leading to the formation of Mg–FSA complex ions. The dominant complex ion species in [C_2epyr]Mg-x is believed to be $[Mg(FSA)_4]^{2-}$. Prior studies comparing FSA^- and $TFSA^-$ complexes reveal that FSA^--containing composites exhibit higher solvation numbers.[38] This study is the first to quantitatively determine the solvation number of Mg^{2+} using Raman spectroscopy. Fig. 4 visualises the structure of the Mg^{2+} complex coordinated with four FSA^- anions, which suggests that Mg^{2+} is densely coordinated.

Ionic conductivity

Fig. 5 shows the Arrhenius plots of the ionic conductivity of the OIPC and OIPC/Mg-salt composites. The ionic conductivity of the OIPC exhibits a jump owing to structural and molecular mobility/diffusion variations associated with T_{s-s} and T_m.[42] The ionic conductivity of [C_2epyr][FSA] used in this study was 8.77 × 10^{-6} S cm^{-1} at 25 °C, which is relatively high among OIPCs. The ionic conductivity of [C_2epyr]Mg-x increased with the addition of the Mg salt, peaked at a certain value, and then decreased. When x = 2.5–7.5, ionic conductivity followed a linear trend up to T_m and then exhibited an upper convex curve at higher temperatures, indicating a Vogel–Fulcher–Tammann

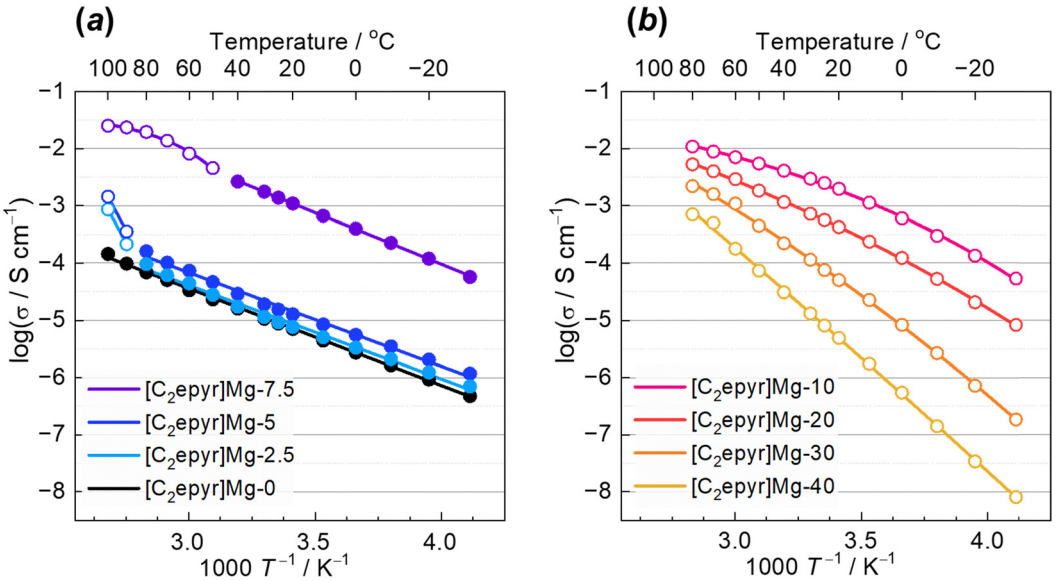

Fig. 5 Arrhenius plots of ionic conductivity for [C_2epyr]Mg-x ((a) x = 0, 2.5, 5, 7.5 and (b) x = 10, 20, 30, 40). Open plots: liquid, closed plots: solid.

(VFT)-type dependence. The discontinuous changes in ionic conductivity differed from the broad T_m values observed in the DSC measurements. When x = 2.5, 5, and 7.5, inflection points in ionic conductivity were observed at 80, 80, and 40 °C, respectively, differing from the T_m values obtained in the DSC measurements.

Nishikawa *et al.* measured the temperature dependence of the spin–spin relaxation times (T_2) of ^{1}H and ^{19}F nuclei in [C_2epyr][FSA] using a low-frequency pulsed NMR apparatus, and observed discontinuous jumps in ^{1}H-T_2 and ^{19}F-T_2 at approximately 27 °C that were not detected by DSC. The authors thus proposed the formation of two phases: a PC phase and a surface phase that develops to relax the surface stress, leading to the emergence of heterogeneous diffusion dynamics.[43]

In this study, discontinuous changes in ionic conductivity were observed in a region not detected by DSC. This finding suggests that AC impedance measurements captured the presence of heterogeneous dynamics.

Table S2 (ESI†) summarises the E_a values of the OIPC and OIPC/Mg-salt composites for their ionic conductivity. The E_a of pure [C_2epyr][FSA] was 14.1 kJ mol^{-1}, while those of composites with x = 2.5, 5, and 7.5 were 13.6, 13.6, and 15.0 kJ mol^{-1}, respectively. In the solid state, E_a remained nearly constant regardless of the salt concentration; by contrast, in the liquid state, E_a increased with the Mg-salt concentration. Although the E_a for ionic conductivity in the liquid phase should ideally be determined using the VFT equation, in this study, the E_a values were estimated by fitting the data to the Arrhenius equation for simplicity. As the fitting yielded high R^2 values, we consider this approach to be reasonable for capturing the overall trend in this study. The lower E_a in the solid state suggests a reduced energy barrier for ion diffusion compared with that in the liquid state. Generally, hopping conduction exhibits a linear behaviour in Arrhenius plots of ionic conductivity.[44] The conduction mechanism in the solid state is likely dominated by hopping conduction, whereas vehicle-type migration is expected to be the primary conduction mechanism in the liquid state.[45] Mori *et al.* prepared organic ionic crystals of [N_{1111}][Mg(μ-η^1–η^1TFSA)$_3$] and reported E_a of 172 kJ mol^{-1} over the temperature range of 10–50 °C.[46] Using the VFT equation, Tominaga *et al.* obtained an E_a of 0.21 eV (20 kJ mol^{-1}) in a system in which 5 mol% Mg(TFSA)$_2$ was added to poly(ethylene carbonate) (PEC).[16] The samples in this study exhibited lower E_a compared with molecular crystals, suggesting higher ionic conductivity. The solid-state electrolytes exhibited E_a values comparable with those of organic solid electrolytes. When $x \geq 10$, the Arrhenius plots showed a characteristic VFT-type behaviour typical of liquid samples. As the Mg-salt concentration increased, the behaviour became more linear, whereas ionic conductivity decreased. Matsumoto *et al.* reported that ionic conductivity in [C_2mim][FSA] composites with NaFSA was viscosity-dependent.[34] The increased viscosity of [C_2epyr]Mg-x owing to Mg-salt addition suggests a similar trend.

Fig. S2 (ESI†) shows the relationship between the Mg-salt concentration and ionic conductivity of the composites at 0, 25, and 60 °C. At 25 °C, the ionic conductivities of composites with x = 5 and 10 were 1.54 × 10^{-5} and 1.78 × 10^{-3} S cm^{-1}, respectively. In our previous study, the doping of Mg(TFSA)$_2$ into [C_2epyr][TFSA] at a concentration of 5 mol% resulted in an ionic conductivity of 6.87 × 10^{-9} S cm^{-1} at 25 °C. In contrast, [C_2epyr]Mg-5, which incorporates a different anion species (FSA), exhibited a significantly higher ionic conductivity. These results indicate that the FSA-based system provides enhanced ionic conductivity compared to the TFSA-based counterpart. Yamada *et al.* reported that the ionic conductivity of a [C_2epyr][FSA]/LiFSA (5 mol%) composite was 1.1 × 10^{-4} S cm^{-1} at 25 °C.[19] A comparison between Li- and Mg-added systems at a concentration of 5 mol% showed that Mg exhibited lower ionic conductivity. In solid-state ionics, the diffusion of Mg^{2+} is generally more challenging than that of Li^+.[47] This observation aligns

with the typical trend, indicating that the composite studied here follows general expectations. In the [C_2epyr][FSA]/NaFSA (10 mol%) system, the sample remained solid at 25 °C,[41] suggesting that divalent electrostatic interactions tend to promote system heterogeneity.

Mg transference number

Fig. S3 and S4 (ESI†) present the chronoamperometry results for Mg|[C_2epyr]Mg-x|Mg cells at 25 °C, where [C_2epyr]Mg-x existed in both the solid and liquid states. Owing to the high charge density of Mg^{2+}, its solvation energy and interfacial resistance are relatively high. $t_{Mg^{2+}}$ was calculated using the I_s/I_0 ratio. The average $t_{Mg^{2+}}$ values for solid-state samples (x = 2.5, 5, and 7.5) were 0.34, 0.28, and 0.26, respectively. As the Mg-salt concentration increased, $t_{Mg^{2+}}$ decreased, suggesting an increase in the liquid component. For liquid-state samples (x = 10, 20, 30, and 40), the $t_{Mg^{2+}}$ values were 0.03, 0.11, 0.154, and 0.149, respectively. Fig. S5 (ESI†) illustrates the relationship between $t_{Mg^{2+}}$ and Mg-salt concentration. As the Mg-salt concentration increased, $t_{Mg^{2+}}$ showed an increasing trend. This result indicates that excessive Mg-salt concentrations lead to increased viscosity and reduced ionic conductivity, even when a large amount of Mg^{2+} is present in the electrolyte. Matsumoto *et al.* reported a similar trend in a composite of [C_3mpyr][FSA] and NaFSA.[48]

The Li transference number (t_{Li+}) of a [C_2epyr][FSA]/LiFSA (5 mol%) composite was reported to be 0.27 at 60 °C,[19] which is comparable with that of the solid-state electrolytes in this study. In a previous study, a [C_2epyr][FSA]/$Mg(TFSA)_2$ composite exhibited $t_{Mg^{2+}}$ values of 0.29 (solid, 5 mol%) and 0.019 (liquid, 15 mol%) at 60 °C.[26] Similar to this study, the solid-state crystals in the present work demonstrated higher $t_{Mg^{2+}}$, suggesting that PC phases enhance Mg^{2+} transport compared with liquid phases.

Fig. 6 illustrates the relationship between the ionic conductivity and $t_{Mg^{2+}}$ of the composites. Generally, these properties exhibit a trade-off relationship; hence, achieving both high ionic conductivity and a high transference number simultaneously is typically challenging. Ionic conductivity is generally enhanced when both cations and anions are mobile. In contrast, when only cations are mobile—that is, when the cation transference number is high—the total number of mobile ionic species is limited, which tends to result in a decrease in overall ionic conductivity. Tominaga *et al.* reported that both ionic conductivity and t_{Li+} increased with higher Li-salt concentrations in PEC and polycarbonate electrolytes with different side-chain groups.[49] The addition of high concentrations of Li salt to PEC resulted in a decrease in E_a of ionic conductivity, leading to a conduction mechanism distinct from that observed at lower salt concentrations. Furthermore, the T_g of PEC decreased upon Li-salt addition, reaching its lowest value in the high-concentration region. In highly concentrated PEC electrolytes, the system becomes quantitatively dominated by the salt, a phenomenon known as 'polymer-in-salt'. In this state, ion mobility is less correlated with the segmental motion of the polymer, giving rise to a decoupled ion conduction mechanism.[49]

In this study, the solid-state electrolytes of [C_2epyr]Mg-x exhibited superior properties compared with conventional ionic liquid electrolytes. The presence of the PC phase appears to effectively break the conventional trade-off relationship,

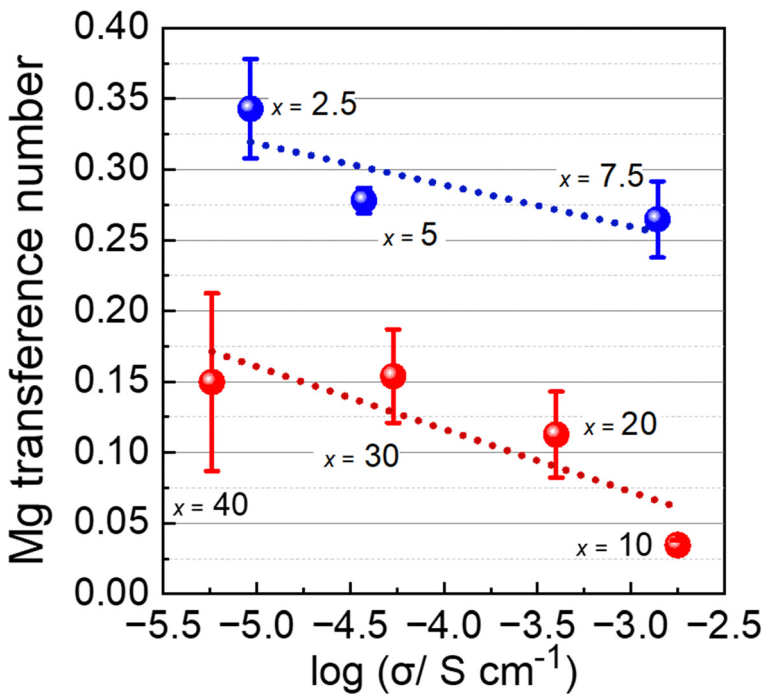

Fig. 6 Relationship between the Mg-ion transference number and ionic conductivity of [C_2epyr]Mg-x at 25 °C (blue: solid, red: liquid, error bars represent standard deviations from the mean).

enabling the co-existence of a high $t_{Mg^{2+}}$ and high ionic conductivity. This finding suggests a new direction for electrolyte design utilising the PC phase. However, the exact role of the PC phase in Mg-ion conduction remains unclear. Philippi *et al.* screened various anions using both theoretical and experimental approaches to identify Li battery electrolytes with high t_{Li+}.[50] The authors hypothesised that maximising Li mobility requires matching the coordination tendencies of the solvent and anion. This balanced selection prevents either coordination site from being overly favoured, potentially facilitating Li hopping. In the present study, Mg-ion conduction was observed within a relatively large coordination environment with a solvation number of 4.0. Because the activation energy remained constant in the PC phase, a favourable conduction mechanism for Mg ions may operate within this phase.

Thermal stability

Fig. S6 (ESI†) presents the thermal stability of [C_2epyr]Mg-5 and [C_2epyr]Mg-10 based on the isothermal TG measurements. The weight change of [C_2epyr]Mg-*x* was measured after being held at 60, 80, or 100 °C for 2 h. [C_2epyr]Mg-5 exhibited no weight loss at 60 °C; however, at 80 and 100 °C, its weight decreased by approximately 0.5% and 1.0%, respectively. By contrast, [C_2epyr]Mg-10 exhibited weight loss even at 60 °C, with reductions of approximately 0.7%, 1.4%, and 1.9% at 60, 80, and 100 °C, respectively. The sample containing 10 mol% Mg salt exhibited a higher decomposition rate and was less thermally stable. Both samples showed limited thermal stability, posing challenges for practical application in devices.

Kerner *et al.* reported that although pure [C_2mim][FSA] (1-ethyl-3-methylimidazolium bis(fluorosulfonyl)amide) exhibited no significant weight change at 125 °C in isothermal TG measurements, the addition of 10 mol% LiFSA resulted in a pronounced weight reduction.[37] A similar trend was observed in the present study, where the addition of $Mg(FSA)_2$ led to decreased thermal stability in the composites. Analysis of the decomposition mechanism of Mg conductors bearing $Mg(TFSA)_2$ as the anion *via* Raman spectroscopy and density functional theory calculations has revealed that increasing the number of anions coordinated to Mg^{2+} and, thus, the solvation number is essential for mitigating anion decomposition.[51] Although the exact cause of the observed weight loss remains unclear, we believe that the decomposition of FSA anions contributes to this phenomenon.

Redox behaviour of Mg

Fig. 7 presents the CV measurement results of [C_2epyr]Mg-5. A reduction current associated with the reduction of Mg^{2+} was observed at potentials below 0 V *versus* Mg/Mg^{2+}, while an oxidation current corresponding to the oxidation of Mg was detected at approximately 1.5 V *versus* Mg/Mg^{2+}. These redox reactions suggest that Mg was reversibly deposited on and stripped from the Pt electrode surface.

FSA^- is known to form an SEI layer through reductive decomposition on the electrode surface.[26] The SEI layer suppresses excessive electrolyte decomposition and stabilises

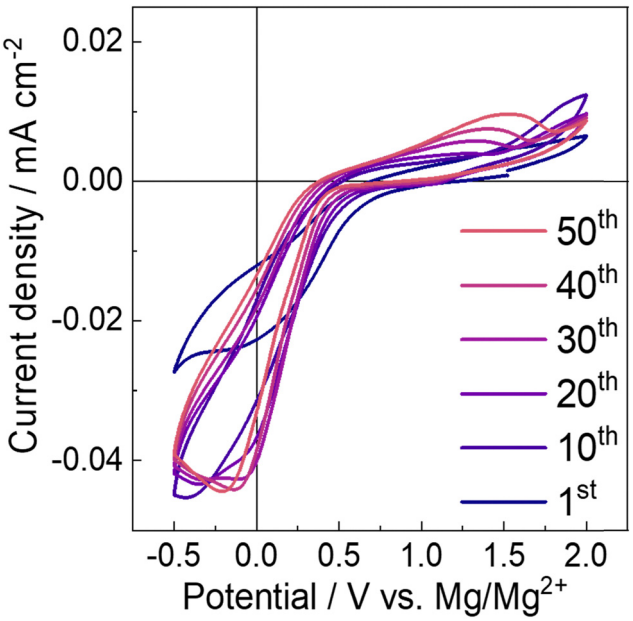

Fig. 7 Cyclic voltammograms of [C_2epyr]Mg-5 at 60 °C.

reversible redox reactions, indicating that the SEI layer forms during the first cycle and that Mg redox reactions are supported from the 10th cycle onwards. Controlling the dissociation degree of the Mg salt is crucial when employing OIPC as a Mg-ion conductor.

Using a similar organic electrolyte, Ab Aziz *et al.* confirmed the deposition and stripping behaviour of Mg in a composite electrolyte consisting of PEC with 40 mol% $Mg(TFSA)_2$. The authors reported that Mg deposition occurred at voltages exceeding 2 V.[16] Higashi *et al.* demonstrated Mg^{2+} conduction *via* the inorganic molecule $Mg(BH_4)(NH_2)$, predicting that $Mg(BH_4)(NH_2)$ behaves as a bandgap insulator with ionic bonding characteristics. Their CV measurements confirmed the reversible redox behaviour of Mg in this material.[52]

Fig. S7 (ESI†) displays the XPS results of the Pt surface after the CV measurements. For verification, measurements were also performed on a polished Mg plate. Peaks corresponding to metallic Mg (Mg 2p, Mg 2s) appeared at positions similar to those of metallic Mg, suggesting the possibility of Mg deposition. This study, which follows prior research on [C_2epyr][FSA]/$Mg(TFSA)_2$, provides further evidence that reversible Mg redox behaviour requires FSA-based anions. The XPS results also suggest that the redox behavior observed in the CV measurements may originate from Mg within the FSA anion-based system. In the future, the cation structure of OIPCs needs to be optimized to improve the Coulombic efficiency of the Mg redox reaction.

Conclusions

In this study, Mg-ion conductors based on the FSA anion were synthesised and characterised by adding $Mg(FSA)_2$ to [C_2epyr][FSA]. [C_2epyr]Mg-10 exhibited a high ionic conductivity

of 1.78 × 10^{-3} S cm^{-1} at 25 °C; however, thermal stability degradation was observed above 60 °C. By contrast, solid-state [C_2epyr]Mg-*x* (*x* = 2.5–7.5) demonstrated both high ionic conductivity and a high $t_{Mg^{2+}}$, suggesting a novel strategy to overcome their conventional trade-off relationship. [C_2epyr]Mg-5 remained stable at 60 °C, and its redox behaviour was confirmed *via* CV measurements.

Furthermore, the solvation number of the conductors was determined to be 4.0, which is relatively high compared with Li- and Na-based systems and reveals a unique solvation behaviour specific to Mg-ion conductors. The results indicate that Mg-ion conductors based on FSA anions possess properties suitable for the electrochemical applications of Mg. However, further improvements in thermal stability are required for the practical implementation of these materials. Future studies should focus on optimising the material composition and exploring new anion frameworks to enhance the thermal stability of such conductors. The findings of this study contribute to the advancement of high-performance Mg-ion conductors and provide critical insights toward the realisation of solid-state Mg batteries.

Author contributions

Y. Hirotsu: synthesis, structural analysis, conceptualization, data curation, formal analysis, investigation, visualization, writing – original draft; M. Kimura: data curation, formal analysis, investigation; S. Nanbu: data curation, formal analysis, validation, supervision; Y. Takeoka: data curation, supervision; M. Rikukawa: data curation, supervision; M. Yoshizawa-Fujita: conceptualization, methodology, data curation, writing – review & editing, visualization, supervision, project administration, funding acquisition.

Data availability

The data that support the findings of this study are available from the corresponding author upon reasonable request.

Conflicts of interest

There are no conflicts to declare.

Acknowledgements

This study was supported by JSPS KAKENHI (22K19072), a research granted from Murata Science and Education Foundation, and a Sophia University Special Grant for Academic Research. We would like to thank Editage (**https://www.editage.jp**) for English language editing.

References

1 J. M. Tarascon and M. Armand, *Nature*, 2001, **414**, 359–367.
2 Y. Q. Chen, Y. Q. Kang, Y. Zhao, L. Wang, J. L. Liu, Y. X. Li, Z. Liang, X. M. He, X. Li, N. Tavajohi and B. H. Li, *J. Energy Chem.*, 2021, **59**, 83–99.
3 H. R. Yao, Y. You, Y. X. Yin, L. J. Wan and Y. G. Guo, *Phys. Chem. Chem. Phys.*, 2016, **18**, 9326–9333.
4 J. Z. Niu, Z. H. Zhang and D. Aurbach, *Adv. Energy Mater.*, 2020, **10**, 2000697.
5 E. Kohan, R. Khoshnavazi, M. G. Hosseini, A. Salimi and M. Salami-Kalajahi, *J. Mater. Chem. A*, 2024, **12**, 30190–30248.
6 P. W. Jaschin, Y. Gao, Y. Li and S. H. Bo, *J. Mater. Chem. A*, 2020, **8**, 2875–2897.
7 M. Matsui, *J. Power Sources*, 2011, **196**, 7048–7055.
8 L. K. Chellappan, J. Kvello, J. R. Tolchard, P. I. Dahl, S. M. Hanetho, R. Berthelot, A. Fiksdahl and K. Jayasayee, *ACS Appl. Energy Mater.*, 2020, **3**, 9585–9593.
9 N. T. M. B. Akhila Das, P. Sreeram, M. J. Jabeen Fatima, J. D. Joyner, V. K. Thakur, A. Pullanchiyodan, J.-H. Ahn and P. Raghavan, *Coord. Chem. Rev.*, 2024, **502**, 215593.
10 P. J. Lian, B. S. Zhao, L. Q. Zhang, N. Xu, M. T. Wu and X. P. Gao, *J. Mater. Chem. A*, 2019, **7**, 20540–20557.
11 D. R. MacFarlane and M. Forsyth, *Adv. Mater.*, 2001, **13**, 957–966.
12 Z. Li, J. Fu, X. Zhou, S. Gui, L. Wei, H. Yang, H. Li and X. Guo, *Adv. Sci.*, 2023, **10**, 2201718.
13 S. Ramalingaiah, D. S. Reddy, M. J. Reddy, E. Laxminarsaiah and U. V. S. Rao, *Mater. Lett.*, 1996, **29**, 285–289.
14 K. M. Anilkumar, B. Jinisha, M. Manoj and S. Jayalekshmi, *Eur. Polym. J.*, 2017, **89**, 249–262.
15 Y. Pang, Y. Zhu, F. Fang, D. Sun and S. Zheng, *J. Mater. Sci. Technol.*, 2023, **161**, 136–149.
16 A. Ab Aziz and Y. Tominaga, *Ionics*, 2018, **24**, 3475–3481.
17 J. M. Pringle, P. C. Howlett, D. R. MacFarlane and M. Forsyth, *J. Mater. Chem. A*, 2010, **20**, 2056–2062.
18 H. J. Zhu, D. R. MacFarlane, J. M. Pringle and M. Forsyth, *Trends Chem.*, 2019, **1**, 126–140.
19 H. Yamada, Y. Miyachi, Y. Takeoka, M. Rikukawa and M. Yoshizawa-Fujita, *Electrochim. Acta*, 2019, **303**, 293–298.
20 M. Yoshizawa-Fujita, H. Yamada, S. Yamaguchi, H. Zhu, M. Forsyth, Y. Takeoka and M. Rikukawa, *Batteries Supercaps*, 2020, **3**, 884–891.
21 T. Ootahara, K. Hatakeyama-Sato, M. L. Thomas, Y. Takeoka, M. Rikukawa and M. Yoshizawa-Fujita, *ACS Appl. Electron. Mater.*, 2024, **6**, 5866–5878.
22 J. Sunarso, Y. Shekibi, J. Efthimiadis, L. Y. Jin, J. M. Pringle, A. F. Hollenkamp, D. R. MacFarlane, M. Forsyth and P. C. Howlett, *J. Solid State Electron.*, 2012, **16**, 1841–1848.
23 M. Yoshizawa-Fujita, S. Kubota and S. Ishimoto, *Front. Energy Res.*, 2022, **10**, 854090.
24 X. Wang, H. Zhu, G. W. Greene, Y. Zhou, M. Yoshizawa-Fujita, Y. Miyachi, M. Armand, M. Forsyth, J. M. Pringle and P. C. Howlett, *Adv. Mater. Technol.*, 2017, **2**, 1700046.
25 Y. Wang and D. Rochefort, *J. Phys. Chem. C*, 2024, **128**, 16343–16352.
26 Y. Hirotsu, R. Sekiguchi, Y. Takeoka, M. Rikukawa and M. Yoshizawa-Fujita, *Bull. Chem. Soc. Jpn.*, 2024, **97**, uoae101.

27 M. J. Frisch, G. W. Trucks, H. B. Schlegel, G. E. Scuseria, M. A. Robb, J. R. Cheeseman, G. Scalmani, V. Barone, G. A. Petersson, H. Nakatsuji, X. Li, M. Caricato, A. V. Marenich, J. Bloino, B. G. Janesko, R. Gomperts, B. Mennucci, H. P. Hratchian, J. V. Ortiz, A. F. Izmaylov, J. L. Sonnenberg, D. Williams-Young, F. Ding, F. Lipparini, F. Egidi, J. Goings, B. Peng, A. Petrone, T. Henderson, D. Ranasinghe, V. G. Zakrzewski, J. Gao, N. Rega, G. Zheng, W. Liang, M. Hada, M. Ehara, K. Toyota, R. Fukuda, J. Hasegawa, M. Ishida, T. Nakajima, Y. Honda, O. Kitao, H. Nakai, T. Vreven, K. Throssell, J. A. Montgomery Jr., J. E. Peralta, F. Ogliaro, M. J. Bearpark, J. J. Heyd, E. N. Brothers, K. N. Kudin, V. N. Staroverov, T. A. Keith, R. Kobayashi, J. Normand, K. Raghavachari, A. P. Rendell, J. C. Burant, S. S. Iyengar, J. Tomasi, M. Cossi, J. M. Millam, M. Klene, C. Adamo, R. Cammi, J. W. Ochterski, R. L. Martin, K. Morokuma, O. Farkas, J. B. Foresman and D. J. Fox, Gaussian, Inc., Wallingford CT, 2016.
28 J. Evans, C. A. Vincent and P. G. Bruce, *Polymer*, 1987, **28**, 2324–2328.
29 K. M. Pozyczka, *Electrochim. Acta*, 2022, **424**, 140683.
30 P. J. Timmermans, *J. Phys. Chem. Solids*, 1961, 1–8.
31 R. Yunis, A. F. Hollenkamp, C. Forsyth, C. M. Doherty, D. Al-Masri and J. M. Pringle, *Phys. Chem. Chem. Phys.*, 2019, **21**, 12288–12300.
32 L. Kufel, I. E. Gunathilaka, M. Forsyth and J. M. Pringle, *J. Phys. Chem. C*, 2024, **128**, 14216–14228.
33 H. Ueda, N. Saito, A. Nakanishi, H. J. Zhu, R. Kerr, F. Mizuno, P. C. Howlett and M. Forsyth, *Mater. Today Phys.*, 2024, **43**, 101395.
34 K. Matsumoto, T. Hosokawa, T. Nohira, R. Hagiwara, A. Fukunaga, K. Numata, E. Itani, S. Sakai, K. Nitta and S. Inazawa, *J. Power Sources*, 2014, **265**, 36–39.
35 D. Monti, E. Jonsson, A. Boschin, M. R. Palacin, A. Ponrouch and P. Johansson, *Phys. Chem. Chem. Phys.*, 2020, **22**, 22768–22777.
36 T. Watkins and D. A. Buttry, *J. Phys. Chem. B*, 2015, **119**, 7003–7014.
37 M. Kerner, N. Plylahan, J. Scheers and P. Johansson, *Phys. Chem. Chem. Phys.*, 2015, **17**, 19569–19581.
38 K. Fujii, H. Hamano, H. Doi, X. D. Song, S. Tsuzuki, K. Hayamizu, S. Seki, Y. Kameda, K. Dokko, M. Watanabe and Y. Umebayashi, *J. Phys. Chem. C*, 2013, **117**, 19314–19324.
39 K. Fujii, T. Nonaka, Y. Akimoto, Y. Umebayashi and S. Ishiguro, *Anal. Sci.*, 2008, **24**, 1377–1380.
40 T. Carstens, A. Lahiri, N. Borisenko and F. Endres, *J. Phys. Chem. C*, 2016, **120**, 14736–14741.
41 Y. Hirotsu, M. L. Thomas, Y. Takeoka, M. Rikukawa and M. Yoshizawa-Fujita, *Sci. Technol. Adv. Mater.*, 2025, **26**, 2466417.
42 S. J. Pas, J. Huang, M. Forsyth, D. R. MacFarlane and A. J. Hill, *J. Chem. Phys.*, 2005, **122**, 064704.
43 K. Nishikawa, K. Fujii, K. Matsumoto, H. Abe and M. Yoshizawa-Fujita, *Bull. Chem. Soc. Jpn.*, 2024, **97**, uoae088.
44 E. A. Arkhipova, A. S. Ivanov, K. I. Maslakov, S. V. Savilov and V. V. Lunin, *Electrochim. Acta*, 2019, **297**, 842–849.
45 B. Koo, H. Lee, K. Park, S. Hwang and H. Lee, *Bull. Korean Chem. Soc.*, 2024, **45**, 92–100.
46 S. Mori, T. Obora, M. Namaki, M. Kondo and M. Moriya, *Inorg. Chem.*, 2022, **61**, 7358–7364.
47 Y. Shao, M. Gu, X. Li, Z. Nie, P. Zuo, G. Li, T. Liu, J. Xiao, Y. Cheng, C. Wang, J. G. Zhang and J. Liu, *Nano Lett.*, 2014, **14**, 255–260.
48 K. Matsumoto, Y. Okamoto, T. Nohira and R. Hagiwara, *J. Phys. Chem. C*, 2015, **119**, 7648–7655.
49 Y. Tominaga, *Polym. J.*, 2017, **49**, 291–299.
50 F. Philippi, M. Middendorf, K. Shigenobu, Y. Matsuyama, O. Palumbo, D. Pugh, T. Sudoh, K. Dokko, M. Watanabe, M. Schonhoff, W. Shinoda and K. Ueno, *Chem. Sci.*, 2024, **15**, 7342–7358.
51 Y. Sun, F. Ai and Y. C. Lu, *Small*, 2022, **18**, e2200009.
52 S. Higashi, K. Miwa, M. Aoki and K. Takechi, *Chem. Commun.*, 2014, **50**, 1320–1322.